Development of a Laser-Produced Plasma X-ray source for Phase-Contrast Radiography of DT Ice layers

N. Izumi, E. Dewald, B. Kozioziemski, O. L. Landen, J. A. Koch

July 30, 2008

LAWRENCE
LIVERMORE
NATIONAL
LABORATORY

Disclaimer

This document was prepared as an account of work sponsored by an agency of the United States government. Neither the United States government nor Lawrence Livermore National Security, LLC, nor any of their employees makes any warranty, expressed or implied, or assumes any legal liability or responsibility for the accuracy, completeness, or usefulness of any information, apparatus, product, or process disclosed, or represents that its use would not infringe privately owned rights. Reference herein to any specific commercial product, process, or service by trade name, trademark, manufacturer, or otherwise does not necessarily constitute or imply its endorsement, recommendation, or favoring by the United States government or Lawrence Livermore National Security, LLC. The views and opinions of authors expressed herein do not necessarily state or reflect those of the United States government or Lawrence Livermore National Security, LLC, and shall not be used for advertising or product endorsement purposes.

Development of a Laser-Produced Plasma X-ray source for Phase-Contrast Radiography of DT Ice layers

N. Izumi, E. Dewald, B. Kozioziemski, O. L. Landen, J. A. Koch

Lawrence Livermore National Laboratory
P.O. Box 808, Livermore CA, 94550 USA

Abstract

Refraction enhanced x-ray phase contrast imaging is crucial for characterization of deuterium-tritium (DT) ice layer roughness in optically opaque inertial confinement fusion capsules. To observe the time development of DT ice roughness over ~ second timescales, we need a bright x-ray source that can produce an image faster than the evolution of the ice surface roughness. A laser produced plasma x-ray source is one of the candidates that can meet this requirement. We performed experiments at the Janus laser facility at Lawrence Livermore National Laboratory and assessed the characteristics of the laser produced plasma x-ray source as a potential backlight for *in situ* target characterization.

I. INTRODUCTION

Our current strategy for producing smooth DT ice layers inside beryllium capsules is to rapidly (in 10-30 sec) cool the DT ice from just below the triple point temperature to the required 1.5K below the triple point just before shooting the target [1-3]. To characterize the ice layer just after the rapid cool requires ~ few-second time resolution. Because beryllium shells are opaque to optical light, we cannot use optical microscopy. Current laboratory micro-focus x-ray tubes do not provide sufficient brightness to produce useful x-ray phase-contrast radiographs over these time scales. Therefore we have explored the possible use of the Janus laser facility to provide bright flash radiographs of a rapidly-cooled layer. We irradiated Au, Pd, Ti, and Sc targets with 5-ns, 300-J, 527-nm laser light. We measured absolute x-ray conversion efficiency and x-ray spot sizes using absolutely-calibrated imaging plates.

II. X-RAY REFRACTION-ENHANCED IMAGING

In order to image the interior of the beryllium capsule (typically 100 μm wall thickness), x-ray energies have to be higher than 2 keV. Because x-ray absorption in DT ice is negligible, the interface between the DT ice layer and the DT gas region can not be observed with conventional absorption radiography. X-ray Refraction-Enhanced Imaging (REI) is a technique that can observe material boundaries of objects that are transparent to x-rays. In the x-ray region, the refractive index of solid density material is slightly lower than that of gas. Therefore, x-rays passing through the ice-gas boundary at shallow incidence angles are slightly deflected to the gas side. Figure 1 shows a schematic of x-ray refraction at the DT-ice gas boundary. Virtually parallel rays from a small x-ray

source pass though the equator of the spherical boundary with shallow angles of incidence. Therefore, even a small refractive index jump across the boundary can deflect the beam and produce a characteristic dark/light band structure in the projected image. Through analytical calculation of the refraction at a spherical boundary, the dark band width in the image plane is [4]

$$i_c = 3 \left[\frac{R}{2pq/(p+q)} \right]^{1/3} \Delta n^{2/3} q \qquad (1),$$

$$\Delta n = \frac{2(n_1 - n_2)}{n_1 + n_2}$$

where R is the radius of the spherical boundary, p and q are the source and detector distances, and n_1 and n_2 are the refractive indices of the gas and ice regions, respectively. For example, when the ice density is 0.25 g/cm^3, the gas density is 3×10^{-4} g/cm^3, and the x-ray energy is 3.2 keV, Δn is about 4 ×10^{-6}. If we set p and q to 2000 mm and 90 mm respectively, the expected width of the dark band of a 1 mm radius boundary is 12 μm on detector plane.

To obtain the distinctive dark band by REI, the geometry of the experimental setup has to satisfy several constraints. First of all, the dark fringe width i_c has to be larger than the resolution of the detector. For the case of above, the detector resolution has to be better than 12 μm. Second, to suppress the smearing of the dark band due to penumbral blur, the angular divergence of the rays on the object has to be small. The

3

angular divergence of rays from a finite source size σ is given by σ/p. This angle has to be smaller than a specific deflection angle θ_c given by [4],

$$\theta_c = 2 \left[\frac{R}{2pq/(p+q)} \right]^{1/3} \Delta n^{2/3}$$

(2),

For the case above, the expected deflection angle θ_c is about 90 μradian. Therefore the stand off distance p has to be $\sim 10^4$ times larger than the source size σ. The absolute x-ray flux on the detector scales with $(p+q)^{-2}$. This constrains the maximum distance from the source to the detector.

Figure 2 shows the typical setup for REI. In principle, there are two geometrical setups which satisfy the constraints. The first solution is a large magnification setup, which has small p and large q (Fig. 2(a)). In this case, the source size has to be small (~ 4 μm) to suppress penumbral blur but the requirement for detector resolution is relaxed. The other solution is a low magnification setup with large p and small q. The long stand off distance p allows the use of a relatively large source. However, higher spatial resolution is required at the detector ($\sim$ few μm).

Laser-produced plasma sources are typically tens-of-microns in diameter, and so are unsuitable for high-magnification REI unless the source size is restricted with a pinhole. An alternative is to use the entire source with a low-magnification geometry. Figure 3 shows a diagram of experiment parameter optimization [5]. There is an optimal x-ray energy that satisfies the requirements of spatial resolution, dark band contrast, and signal-to-noise. Low energy x-rays have larger refraction angles, but are strongly

absorbed by the beryllium shell along the ~ 350 μm (thin shell) to ~ 950 μm (thick shell) path including Be vacuum windows. Conversely, higher-energy x-rays have more transmission through the beryllium shell and windows, but the refraction angles are small due to the smaller refractive index jump, and more photons detected per resolution element are required. The optimal x-ray energy that minimizes the required x-ray energy conversion is found to be 3 to 5 keV, and the standoff distances p and q can be found by matching the expected contrast and resolution to that currently obtained with long-exposure micro-focus tube images, assuming a 100 μm source size. For the low-magnification setup, the optimal combination of p and q are ~ 2 m and 2 cm, respectively.

III. EXPERIMENTS

We performed experiment at the Janus laser facility at Lawrence Livermore National Laboratory in order to determine if the x-ray conversion efficiency and source size of x-ray sources generated by laser irradiation of thin metal foil targets are adequate according to Fig. 3. Figure 4 shows the experimental setup. The targets were irradiated by a frequency-doubled Nd glass laser ($\lambda = 532$ nm, pulse width ~ 5 ns, 300 joules) at an intensity of 8×10^{14} watt/ cm^2 and at an angle of incidence of 45 degrees. Prior to each shot, the laser spot size on target was monitored by using a microscope objective lens coupled to a CCD.

A) X-ray source size

The x-ray spot size was monitored by an x-ray pinhole camera located at 30 degrees from the target normal. An array of pinholes with 10 μm diameter was placed 5.6

cm from the laser target, and the images were projected onto an imaging plate (FUJI BAS-SR) with a magnification of 5.4. Figure 5 shows the x-ray spot images. The smallest laser spot (~ 40 μm diameter) was observed by an optical microscope objective lens on the first shot of the day, and increased to ~ 90 μm diameter by the fourth shot of the day due to thermal aberrations in the laser amplifiers that increased the laser focal spot size. The observed x-ray spot size (~ 80 μm on the first shot) was larger than the laser spot size due to the hydrodynamic expansion of the laser produced plasma.

B) Absolute x-ray flux measurement

To observe the dark fringe with significant contrast, we need adequate photon statistics per resolution element. The absolute x-ray flux from the laser-produced plasma was measured with an imaging plate (BAS-SR) backing an x-ray filter array. The detector was located 2.3 m from the laser target. Prior to the experiments, the absolute sensitivity of the plate was calibrated using radioactive isotopes at 5.9 keV (^{55}Fe) and 22 keV (^{109}Cd); the spectral sensitivity of the IP for other x-ray energies was extrapolated using a Monte Carlo radiation transport code MCNP5 [6]. The plates were scanned with an imaging plate scanner (FUJI FLA7000); in order to avoid sensitivity changes due to signal fading, all plates were scanned consistently 20 minutes after exposure. The filter materials used for each region are shown in Table 1, and the calculated spectral response is shown in Figure 6. Figure 7 shows typical raw data obtained with a gold target.

The source spectra were inferred by unfolding the experimental data. We modeled the source spectra using 4 parameters: (1) temperature of the continuum emission, (2) intensity of the continuum emission, (3) intensity of the line emission, (4)

6

energy of the line emission. The energy of the line emission was set to M or L line emissions [7, 8] or He-alpha line emission [9] depending on target material. The other 3 parameters were used to fit the intensities of the data in the differentially filtered regions of the image plate. Figure 7 shows the comparison of the raw data and the intensities of the channels numerically generated from the fitted source spectra. Signal intensities of all the channels were well reproduced by the modeled spectra.

Table 2 shows the resulting fit parameters and conversion efficiencies. The slope of the continuum emission was typically 2 keV. In these experiments, the gold target had the maximum conversion efficiency. About 8 % of the laser energy was converted to gold M-band emission between 1.8 ~ 3.5 keV. L-band emission from palladium (~ 3%) and He-alpha emission from titanium and scandium (~ 1%) were weaker than gold M-band.

C) Demonstration of REI with a surrogate capsule

Figure 8 shows the image obtained in a proof-of-principle experiment with a plastic surrogate capsule. A deuterated plastic capsule (2 mm diameter, 100 μm thickness) was located 1940 mm from the laser plasma source. DEF x-ray film was located 90 mm behind the object. Figure 8 also shows the intensity profile of the image near the outer edge. The dark band was observed successfully on the inner surface of the shell. The estimated electron density in the plastic shell was 3.5×10^{23} cm^{-3}, and the refractive index jump Δn at the inner surface was 2.7×10^{-5}. The dark band width estimated by equation (1) at 3 keV is about 42 μm. The observed width of the dark band was approximately 40 μm. This result assures consistency of the analytical modeling.

The observed dark-band profile also confirms that the effective x-ray source size was small enough (~ 100μm) to satisfy the constraint of the angular divergence given by equation 2.

IV. DISCUSSION

The conversion efficiencies obtained from these experiments are plotted in Figure 3. All of the materials used in these experiments satisfy the required conversion efficiencies for REI of the DT ice-gas interface through 950 μm of beryllium layers. The dark band width observed with the surrogate capsule agreed with that of the analytical prediction. However, the dark band width expected from an actual DT ice-gas interface is about 9 μm, and so a high-resolution imaging detector will be required to utilize the relatively large laser-produced plasma x-ray source. It is possible to obtain adequate spatial resolution using a thin transparent scintillator coupled with a microscope objective [10].

ACKNOWLEDGEMENTS

REFERENCES

[1] D. Bittner, et al., "IR layering in a hohlraum", presented at the 13th Target Fabrication

Specialists Meeting, Catalina Island, CA, Nov. 8-11(1999).

[2] M. Martin, et al., Fusion Sci. Technol. 49, 600 (2006).

[3] J. D. Moody, et al., Journal de Physique IV (Proceedings) 133, 863 (2006)

[4] B. J. Kozioziemski, J. A. Koch, et al., J. Appl. Phys. **97**, 063103 (2005)

[5] Jeffrey A. Koch, et al., (to be published)

[6] X-5 Monte Carlo Team, MCNP-A General N-Particle Monte Carlo Transport Code,

Version 5.1.40, Los Alamos national Laboratory, (2005)

[7] D. L. Matthews, E. M. Campbell, et al., J. Appl. Phys. 54, 4260 (1983)

[8] D. W. Phillion, C. J. Haileyl, Phys. Rev. A. 34, 4886 (1986)

[9] A. C. Thompson, et al., *X-RAY DATA BOOKLET Second ed.* (Lawrence Berkeley

National Laboratory, University of California, USA, 2001), pp.1-53 – 1-56

[10] T. Martin, A. Koch, J. Synchrotron Rad. 13, 180 (2006)

FIGURE CAPTIONS

Fig. 1. Refraction of x-rays passing though the DT-ice gas boundary. Since the refractive index of the ice layer is slightly smaller than that of the gas region, rays passing though the boundary are deflected and make a dark band on the projected image. A fraction of the deflected rays make a bright band inside the dark band.

Fig. 2. Typical setups of refraction-enhanced imaging. Contrast of the dark band can be obtained using both high and low magnification setups.

Fig. 3. Required parameters to obtain good image resolution, contrast, and signal-to-noise of the refraction contrast image assuming a 100 μm source diameter. The required conversion efficiencies were calculated assuming a 600 joule laser pulse and an x-ray detector with $\sim 50\%$ quantum efficiency. Data points imposed are conversion efficiencies obtained in this experiment. All the target materials have enough conversion efficiency for REI of DT ice layers.

Fig. 4. Schematic view of experimental setup. Laser spot size was measured by a microscope objective lens coupled to a charge-coupled-device.

Fig. 5. X-ray emission spot observed by the time integrated pinhole camera. The observed spot size was smaller than 100 μm FWHM.

Fig. 6. Spectral sensitivities of the imaging plate backing an array of x-ray filters. Channel A to H were covered with aluminum filters with different thickness. Channel I to P was covered with K edge filters with various materials. Details of the filter compositions are shown in Table 1.

Fig. 7. Typical raw data on gold target shot obtained with the imaging plate (BAS-SR) and the filter array (left). The observed signal levels were consistently explained by modeled x-ray spectrum (right).

Fig. 8. Refraction enhanced image of a plastic surrogate target radiographed onto Kodak DEF film (left). The dark band on the inner surface of the plastic shell was clearly observed, and the measured width (~ 40 μm) was consistent with the analytical prediction (right).

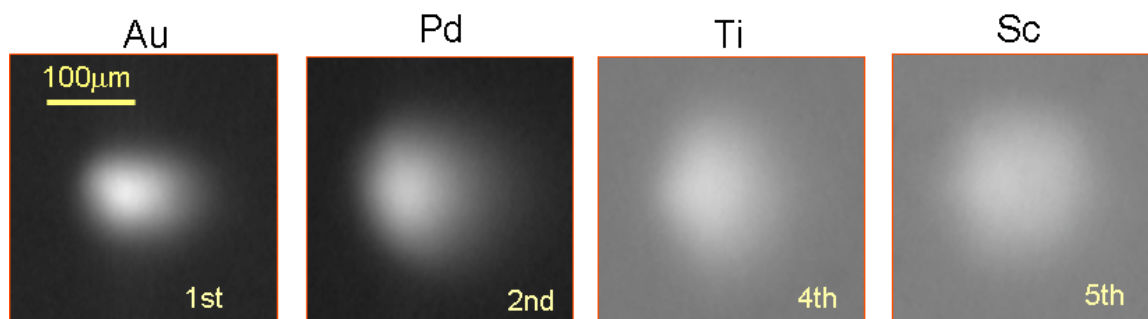Figure 1

(a)

σ

p

q

(b)

σ

p

q

Figure 2

13
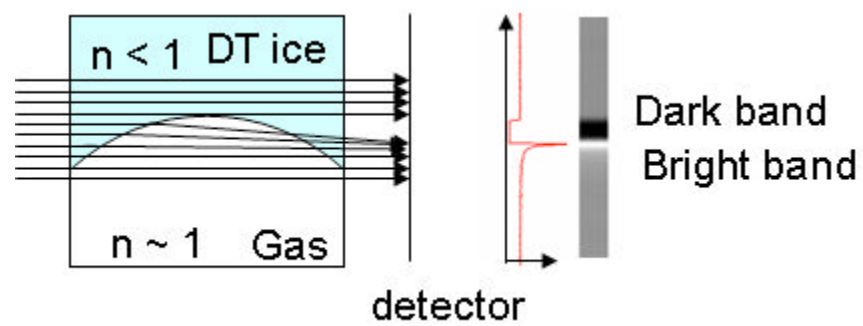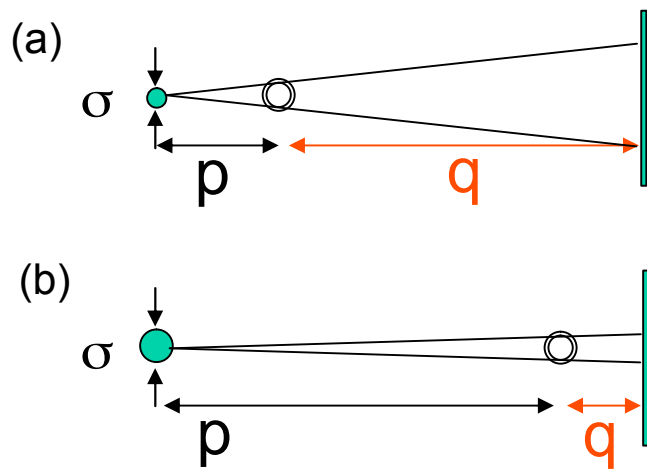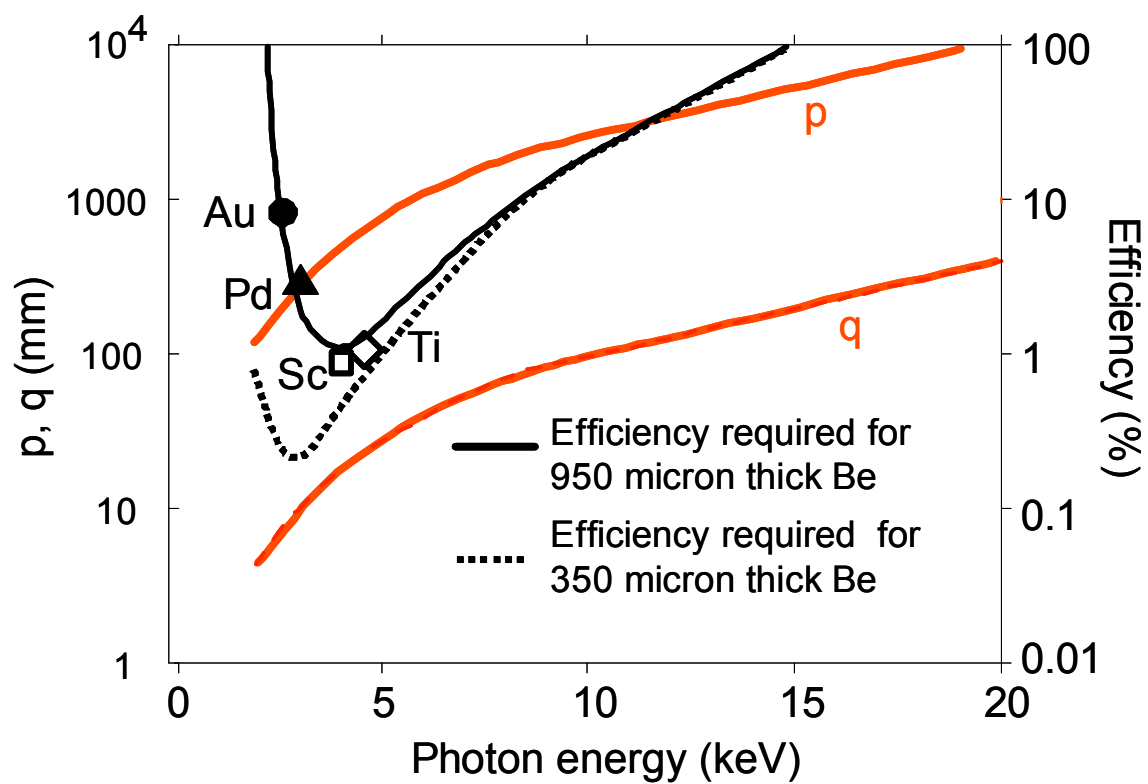
Figure 3

Figure 4

Figure 5

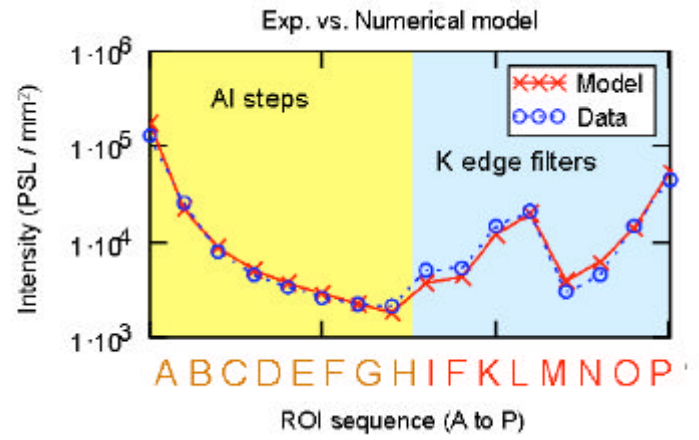16

Figure 6.

Figure 7.

Profile of DEF film image (negative)
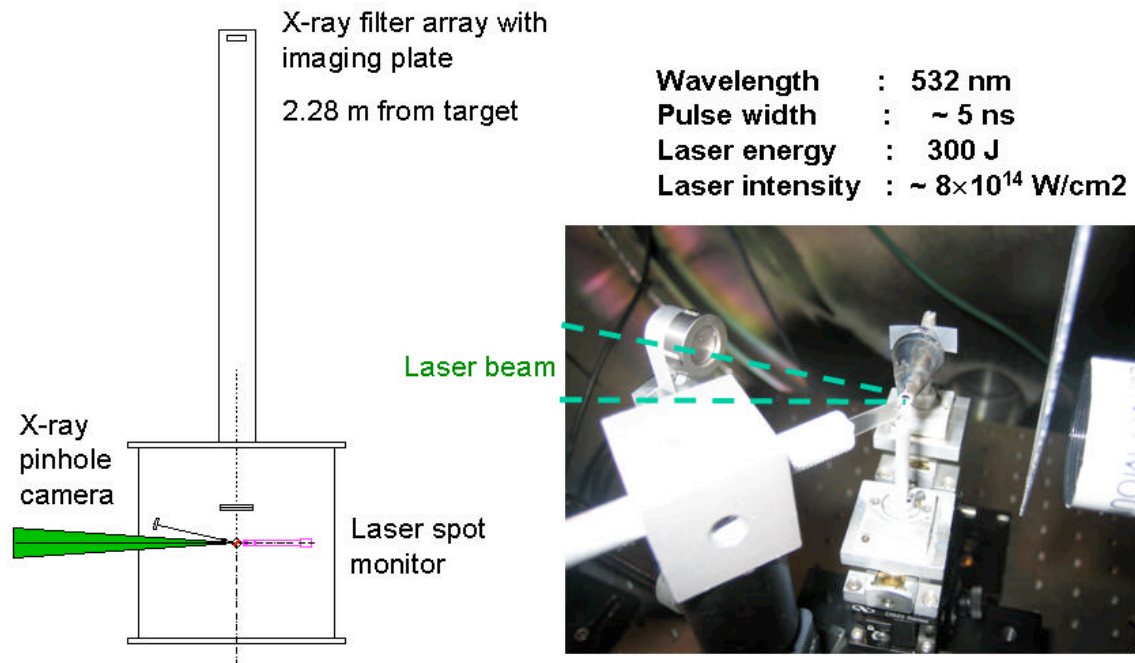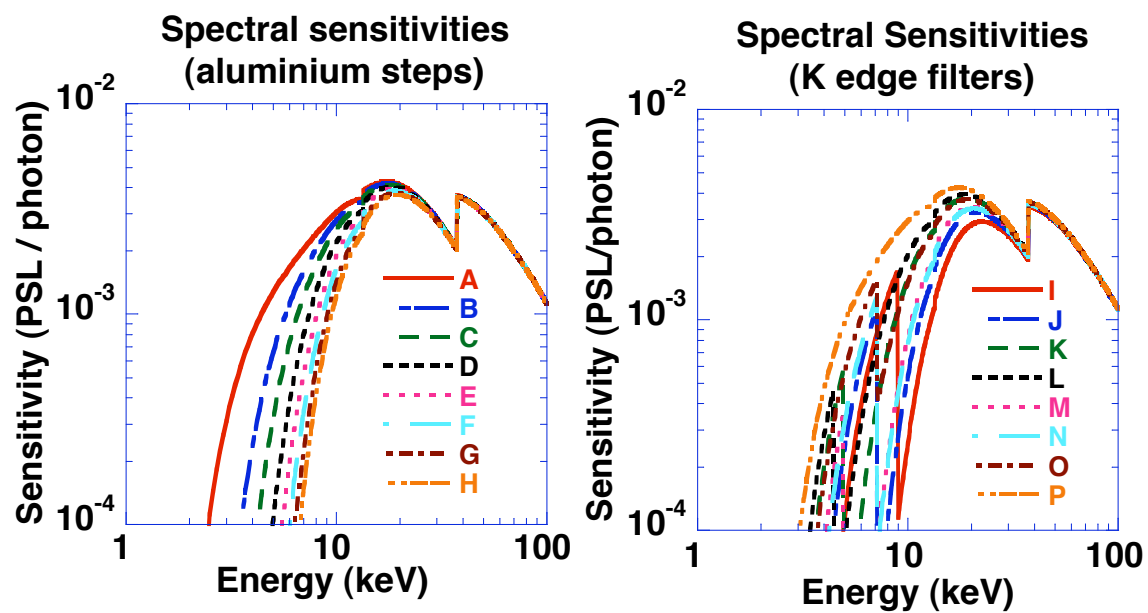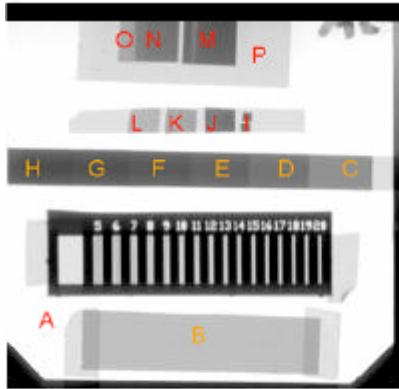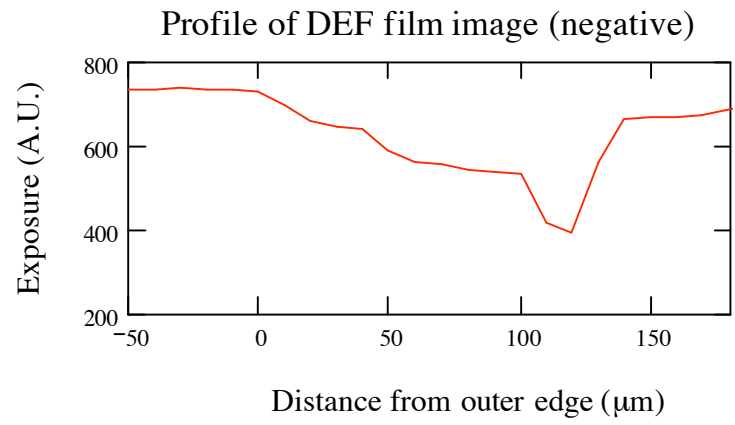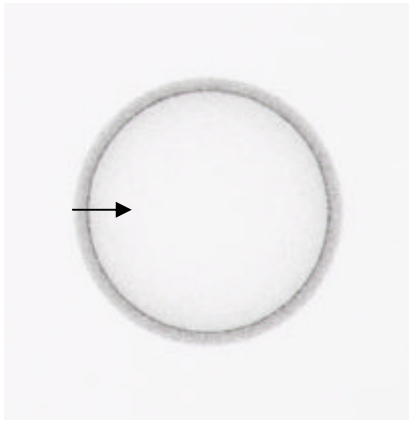
Figure 8.

Table 1. Filter materials used for x-ray flux measurement

Channel	Filters
A	Be 254 μm
B	Al 12.7 μm + Be 254 μm
C	Al 21.3 μm + Be 254 μm + polyester 72.3 μm
D	Al 42.6 μm + Be 254 μm + polyester 72.3 μm
E	Al 63.9 μm + Be 254 μm + polyester 72.3 μm
F	Al 85.2 μm + Be 254 μm + polyester 72.3 μm
G	Al 106.5 μm + Be 254 μm + polyester 72.3 μm
H	Al 127.8 μm + Be 254 μm + polyester 72.3 μm
I	Cu 12.7 μm + Be 254 μm + polyester 72.3 μm
J	Fe 12.7 μm + Be 254 μm + polyester 72.3 μm
K	Ti 12.7 μm + Be 254 μm + polyester 72.3 μm
L	Sc 12.7 μm + Be 254 μm + polyester 72.3 μm
M	Ti 25.4 μm + Be 254 μm + polyester 72.3 μm
N	Fe 10 μm + Be 254 μm + polyester 72.3 μm
O	Fe 5 μm + Be 254 μm + polyester 72.3 μm
P	Be 254 μm + polyester 72.3 μm

Table 2. Experimental results

Target	E_L (J)	Laser spot d. (μm)	$T_{cont.}$ (keV)	E_{cont} (J)	$h\nu_{LINE}$ (keV)	E_{LINE} (J)	Conversion
Au	320	40	2.4	3.6	1.8~3.5	27	8.4 %
Au	136	33	2.4	1.6	1.8~3.5	9.5	7 %
Pd	319	50	1.8	4.9	2.9~3.5	9.6	3 %
Ti	310	90	2.2	3.7	4.7	3.0	1 %
Sc	327	80	1.6	7.6	4.3	3.0	0.9 %

X-ray fluxes were measured 45 degrees from the target normal of the irradiated sides of the targets. X-ray energies shown are flux observed on the IP multiplied by 4π steradian (angular dependence of the x-ray flux was ignored).